AI-Based Tracking of Fast-Moving Alpine Landforms Using High Frequency Monoscopic Time-Lapse Imagery

Hanne Hendrickx[1,2]~~,~~*, Melanie Elias[1]*, Xabier Blanch[1,3]~~, Melanie Elias[1]~~, Reynald Delaloye[2], Anette Eltner[1]

[1]Institute of Photogrammetry and Remote Sensing, TUD Dresden University of Technology, 01062 Dresden, Germany
[2]Department of Geosciences, University of Fribourg, Fribourg, 1700, Switzerland
[3]Department of Civil and Environmental Engineering, Universitat Politècnica de Catalunya, 08034 Barcelona, Spain

Correspondence to: Hanne Hendrickx (hanne.hendrickx@tu-dresden.de~~)~~), Melanie Elias (melanie.elias@tu-dresden.de)

* shared first authorship

Abstract: Active rock glaciers and landslides are ~~critical indicators of permafrost dynamics~~dynamic landforms in high mountain environments, ~~reflecting~~where their geomorphic activity can pose significant hazards, especially in densely populated regions like the European Alps. Moreover, active rock glaciers reflect the long-term thermal state of permafrost and ~~responding~~respond sensitively to climate change. Traditional monitoring methods, such as ~~dGNSS~~in-situ differential Global Navigation Satellite System (GNSS) and ~~permanent installations~~georeferenced Total Station (TS) measurements, face challenges in measuring the rapid movements of these landforms due to environmental constraints and limited spatial coverage. Remote sensing techniques offer improved spatial resolution but often lack the necessary temporal resolution to capture sub-seasonal variations. In this study, we introduce a novel approach utilising monoscopic time-lapse ~~imagery~~image sequences and Artificial Intelligence (AI~~-based algorithms~~) for high-temporal-resolution velocity estimation, applied ~~onto~~to two subsets of ~~monoscopic~~ time-lapse ~~images of~~datasets capturing a fast-moving landslide and rock glacier at the Grabengufer site (Swiss Alps). Specifically, we employed the Persistent Independent Particle tracking (PIPs++) model for 2D image point tracking and the ~~AI-based LightGlue matching algorithm~~image-to-geometry registration to transfer the measured 2D image ~~data~~points into 3D object space and further into ~~4D~~velocity data. For the latter, we use an in-house tool called GIRAFFE, which employs the AI-based LightGlue matching algorithm. This methodology was validated against GNSS and TS surveys, demonstrating its capability to provide spatially and temporally detailed velocity information. Our findings highlight the potential of image-driven methodologies to enhance the understanding of dynamic landform processes, revealing spatio-temporal patterns previously unattainable with conventional monitoring techniques. By leveraging existing time-lapse data, our method offers a cost-effective solution for monitoring various geohazards, from rock glaciers to landslides, with implications for enhancing alpine safety ~~and informing climate change impacts on permafrost dynamics.~~. This study marks the pioneering application of AI-based methodologies in environmental monitoring using time-lapse image data, promising advancements in both research and practical applications within geomorphic studies.

Style Definition: Hyperlink: Font color: Dark Blue

Style Definition: caption11: Font: 12 pt, Not Bold, Italic, Space Before: 6 pt, After: 6 pt, Line spacing: 1.5 lines, Suppress line numbers

Style Definition: Bullets: Outline numbered + Level: 1 + Numbering Style: Bullet + Aligned at: 0.63 cm + Tab after cm + Indent at: 1.27 cm

Style Definition: Revision

1 Introduction

Active rock glaciers are creeping permafrost features (Barsch, 1996; Kääb and Reichmuth, 2005), serving as ~~crucial~~ indicators of permafrost distribution in high mountain environments (Marcer et al., 2017; RGIK, 2023). Their velocity ~~directly reflects the thermal state of the permafrost (Delaloye et al., 2010), with higher flow speeds occurring near permafrost limits~~results

35 from various parameters such as topographic conditions, rock glacier material, and internal structure, and it reflects long-term, temperature driven changes in permafrost structure (Cicoira et al., 2021; Delaloye et al., 2010). Higher creep rates typically occur towards the lower permafrost limits, where mean annual air temperatures approach 0°C (Frauenfelder et al., 2003). They efficiently transport sediment (Delaloye et al., 2010; Kummert and Delaloye, 2018), ~~in acceleration concomitant to rock glacier creep rates becoming more pronounced in a warming climate (Delaloye et al., 2013). The same is true for permafrost-related~~

40 ~~creep features such as landslides~~and this becomes more pronounced as rock glacier creep rates increase in a warming climate (Delaloye et al., 2013; Pellet et al., 2023). The same is true for certain types of landslides, where the primary driver of motion is permafrost creep. ~~(Delaloye and Staub, 2016).~~ This can pose significant geohazards when direct connections to downslope infrastructure exist. Precise monitoring of these fast-moving high-alpine landforms is thus essential for future alpine safety (Hermle et al., 2022), as it provides information about the ~~impact of climate change on creeping mountain permafrost and its~~

45 ~~thermal state~~environmental drivers and enhances process understanding. ~~(RGIK, 2023).~~

The monitoring of fast creeping rock glaciers (>-3 ~~my~~m a⁻¹, Marcer et al. 2021) or landslides is particularly challenging. Traditional techniques that require frequent field access, such as in-situ differential Global Navigation Satellite System (~~dGNSS~~GNSS) measurements, face environmental and logistical obstacles. Permanent GNSS installations can offer displacement observations with millimetre accuracy at a continuous temporal resolution, but they may not have the desired

50 longevity on fast-moving landforms due to extreme cases of block sliding ~~and,~~ rotation, and rockfall, necessitating re-levelling or instrument replacement (Cicoira et al., 2022). Both ~~dGNSS and permanent installations~~GNSS and total station (TS) measurements only measure discrete points, resulting in a limited spatial distribution. However, spatial heterogeneity of landform movement can be expected depending on internal rock glacier structure and terrain characteristics (RGIK, 2023). Improved spatial coverage can be achieved using remote sensing data, such as 3D point clouds derived from Uncrewed Aerial

55 Vehicles (UAV) and Terrestrial or Airborne Laser Scanning (TLS and ALS). These techniques minimize the need for extensive field access, enabling operators to avoid in-person exposure to the fastest-moving areas while still capturing detailed data from these regions. However, these methods often lack the temporal resolution necessary to capture sub-seasonal variations of the landform to its environmental drivers, essential to increase process understanding. Time-lapse imagery or webcam data have the capability to capture the kinematics of alpine landforms with, e.g., hourly resolution. Fixed photogrammetric ~~or~~

60 ~~stereoscopic~~ camera systems, which are increasingly implemented, involve multiple time-lapse cameras to reconstruct high-resolution 3D point clouds similar to those from UAVs or TLS, and at a fraction of the cost ~~(Blanch et al., 2021; Eltner et al., 2017; Ioli et al., 2024).~~(Blanch et al., 2023; Eltner et al., 2017; Ioli et al., 2024, Ulm et al., 2025). Nonetheless, deploying multiple cameras in dynamic alpine environments can be challenging, often requiring wide baselines that complicate point

cloud generation ~~(Ioli et al., 2024).~~(Ioli et al., 2024). Recent studies have demonstrated that metric measurements can be obtained from 2D images alone when a 3D model is available, reducing the need for extensive camera arrays ~~(Altmann et al., 2020; Elias et al., 2023; Wegner et al., 2023)~~(Altmann et al., 2020; Elias et al., 2023; Wegner et al., 2023). Furthermore, monoscopic camera data, which is more readily available than stereo images, often spans a decade or more in the European Alps (Kummert et al., 2018). Generally installed in stable terrain, these cameras tend to have greater longevity than permanent GNSS installations. However, most time-lapse camera systems are highly weather-dependent. Changes in the camera's intrinsic and extrinsic properties caused by thermal variations (e.g., Elias et al., 2020) and external disturbances such as snow and wind are common, significantly affecting the image configuration. Additionally, maintaining a perfectly stable camera position over the long term can be very challenging in a dynamic mountain environment.

Measuring the velocity of boulders ~~within~~in the camera's field of view is possible by ~~establishing~~measuring homologous point correspondences between ~~pairs of points~~ images in an ~~image pair~~a series, a common challenge in computer vision called feature tracking using optical flow-based methods and feature matching (Fortun et al., 2015). Feature tracking is essentially an ~~optimization~~optimisation problem, where the location of highest similarity between a reference template and a template in the destination image is considered a match ~~(e.g., Eltner et al., 2022). Common similarity measures include Normalized Cross-Correlation (NCC) (Heid and Kääb, 2012) and least square matching~~(Eltner et al., 2022). Common similarity measures include Normalised Cross-Correlation (NCC) (Heid and Kääb, 2012) and Least Square Matching ~~(Schwalbe and Maas, 2017). Traditional motion estimation methods face challenges with large displacement, strong illumination changes, and occlusions. Image pre-selection is crucial to minimize shadowing variation (e.g.,~~(LSM, Schwalbe and Maas, 2017). While traditional motion estimation methods are commonly applied in natural hazard management, they face decorrelation challenges with large displacements, strong illumination changes, and occlusions. Image pre-selection is crucial to minimize illumination variations (e.g., selecting images from the same time of day), thereby limiting temporal resolution (How et al., 2020). ~~Additionally, high landform velocities can cause decorrelation and noise when using typical area-based matching algorithms, such as NCC (e.g., CIAS by Kääb and Vollmer, 2000), for tracking features between consecutive surveys.~~

In the era of Artificial Intelligence (AI), traditional feature tracking can leverage the power of Deep Learning. Convolutional Neural Networks (CNNs), ~~widely~~ employed as feature extractors, replace handcrafted features or the use of image intensities or gradients (Hur and Roth, 2020). This approach offers the advantage of representing each pixel with a high-dimensional feature vector, blending distinctiveness and invariance to, for example, appearance changes, thereby enhancing feature robustness over time. ~~This enhances image matching algorithms, as seen with models like SuperGlue (Sarlin et al., 2020)~~This enhances, on the one hand, image feature tracking (e.g., PIPs++ (Zheng et al., 2023), VideoFlow (Shi et al., 2023), Raft (Teed and Deng, 2020)), and, on the other hand, image matching algorithms, as seen with models like SuperGlue (Sarlin et al., 2020), LightGlue (Lindenberger et al., 2023) ~~and~~or LoFTR (Sun et al., 2021).

The goal of this research is to obtain spatio-temporal high-~~quality~~resolution landform velocities from monoscopic time-lapse cameras, verified through ~~permanent~~ permanenting-situ GNSS and ~~dGNSS~~TS surveys. To improve motion estimation in mountain time-lapse image sequences, we tested the deep learning model called Persistent Independent Particle tracking (PIPs++) (Harley et al., 2022; Zheng et al., 2023) to track landslide and rock glacier movements and the AI matching algorithm LightGlue (Lindenberger et al., 2023) ~~to convert 2D image measurements to 3D information (Elias et al., 2023). By analysing a small subset of a large time-lapse image dataset, we automatically extracted velocity information as a proof-of-concept. We demonstrate the potential of new methodologies for managing big data and improving the spatio-temporal understanding of landform movements. Two fast-moving alpine landforms (a landslide and rock glacier at Grabengufer site, Switzerland) were selected as a pilot study area. The ultimate aim is to derive reliable velocity values at high temporal resolution from low-cost monoscopic time lapse cameras, which have not been previously used quantitatively. To achieve this, we developed a workflow applicable to other research sites where validation data is scarce or where traditional remote sensing techniques fall short due to high landform displacements. This approach not only enhances analysis capabilities but also enables the use of basic systems, such as monoscopic cameras, for automatic and cost-effective monitoring and quantification.~~for image-to-geometry registration to transfer 2D image measurements to 3D information implemented in an in-house open source tool, designated GIRAFFE (Geospatial Image Registration And reFErencing). GIRAFFE performs synthetic image rendering from a scaled 3D point cloud and approximates of a linear camera model to fit the perspective of the originally captured 2D image. The method was presented in Elias et al. (2019) with a particular emphasis on image-based water level measurement. The matching was based on handcrafted features utilising the Scale-Invariant Feature Transform (SIFT) operator (Lowe et al., 2004), which is an effective method when the images to be matched have similar perspectives and lighting conditions. To enhance robustness against these conditions, the tool was further developed using the AI-based SuperGlue (Sarlin et al., 2020) matcher (Elias et al., 2022) and demonstrated the potential for multi-modal image-to-geometry registration (Elias et al., 2023). In this study, we employ the stable and open-source LightGlue image matcher. We publish the source code of GIRAFFE to carry out own time-lapse based velocity measurements with our presented approach.

We introduce a novel low-cost image-based remote measurement technology designed for application in challenging and hard-to-access terrains. The proposed method has been validated by processing two subsets from two extensive time-lapse image datasets, converting them into image-based velocity information. Two rapidly moving alpine landforms, a landslide and a rock glacier, were observed at the Grabengufer site in Switzerland. We highlight the potential of these innovative methodologies to manage large datasets effectively and enhance the spatio-temporal understanding of landform dynamics. Our approach not only improves analytical capabilities but also facilitates the use of basic systems, such as monoscopic cameras, for automated, cost-effective monitoring and quantification of landform movements.

2. Study area and dataset description

The study area of Grabengufer consists of two fast-moving alpine landforms (Fig. 1). The upper part (2700 – 2880 m a.s.l.) consists of a landslide moving up to 1.5 m a year and whose crumbling front is observed using a permanently installed webcam (hereinafter named Wcam04). This landform feeds into a rock glacier (2400 – 2600 m a.s.l.), currently moving at a rate of 0.25 to 0.69 meters per day (observed by webcam Wcam05), leading into a gully prone to debris flows (observed by another webcam not used in this study). The site is extensively monitored, with bi-annual dGNSS surveys, several permanent GNSS installation from PermaSense (https://www.permasense.ch/en.html) and Glaciorisk (https://www.glaciorisk.ch/), dozens of fixed reflectors for repeated theodolite measurements, three time-lapse cameras since 2010/2013 (Wcam02, 04, and 05), and three ground surface temperature loggers.

Wcam05 – Rock glacier

Wcam04 – Landslide

Wcam02 – Rock glacier & upper gully
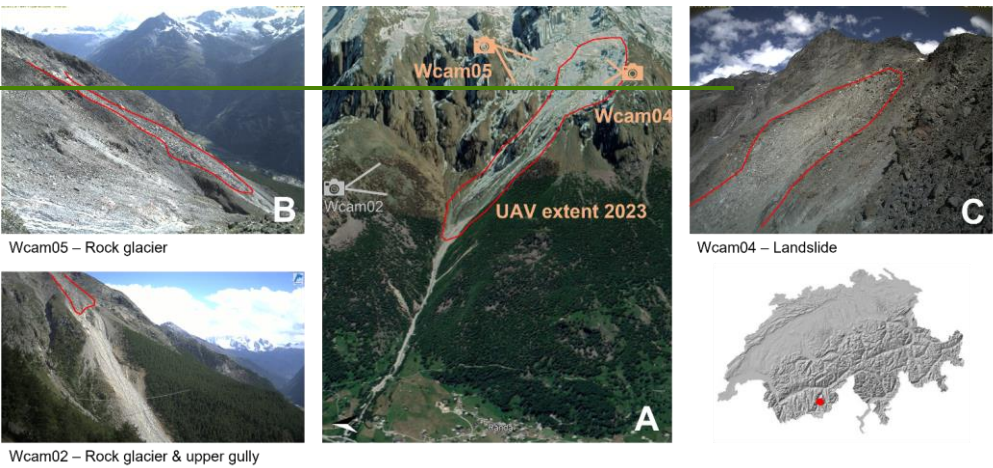
The Grabengufer study area features two fast-moving alpine landforms (Fig. 1a). The upper section (2700 – 2880 m a.s.l.) consists of an extensive deep-seated landslide moving up to 1.5 m a^{-1} (Fig. 1a blue polygon). The landslide is made of in-situ bedrock, fractured by its motion. Its thickness is estimated to be around 30 to 40 m and up to 100 m in the most northern section where it is covered by debris fallen from the Grabenhorn. According to installed Ground Surface Temperature (GST) loggers, its temperature is still below 0° despite recent warming. The southern part of the landslide is frozen and ice saturated (unpublished data). Maximal intra-annual velocities are reached around November and the velocities have multiplied by four (from 0.3 to 1.2 m a^{-1}) between 2009 and 2024. Therefore, permafrost creep is expected to be one of the major drivers of the current motion of the landslide. However, due to the absence of rock glacier morphology, we use the generic term 'landslide'. The frontal section of the southern part of this landslide is very unstable and the source of frequent rock falls. It gradually turns into a very rapid mass movement, referred to as the "(rock glacier) feeding section". Both frontal and feeding sections are monitored by a permanently installed webcam (hereinafter named Wcam04, Fig. 1c orange polygon). The fed rock glacier

(2400 – 2600 m a.s.l., Wcam05, Fig. 1b red polygon) is very active and was considered destabilised during the 1940s and 2000s. As of summer 2023, in-situ measurements indicate that it moves again exceptionally fast at a rate of 0.25 to 0.70 m d$^-$^{1}, marking a third phase of destabilisation. The rock glacier tongue terminates on a very steep slope section leading into a gully prone to debris flows, which is observed by a separate webcam not included in this study. The site is extensively monitored through bi-annual dGNSS surveys (conducted at the end of June and October), several permanent GNSS installations operated by PermaSense (Cicoira et al., 2022) and Canton of Valais (providing continuous data saved as 2-hour means), ten fixed reflectors for repeated TS measurements (approximately once a month), three time-lapse cameras operational since 2010/2013 (Wcam02, Wcam04, and Wcam05), and three GSTs. For this study, we used the monthly TS measurements and a permanent GNSS system installed and operated by the Canton of Valais to validate the velocities derived from the time-lapse image sequences. This GNSS system uses a local fixed reference station in stable terrain located approximately 3 km away and 250 m lower in elevation, to provide accurate differential positioning. The image data analysed in this study was captured by the webcams Wcam04 and Wcam05, powered by solar panels. The characteristics of these webcams are summarised in Table 1.
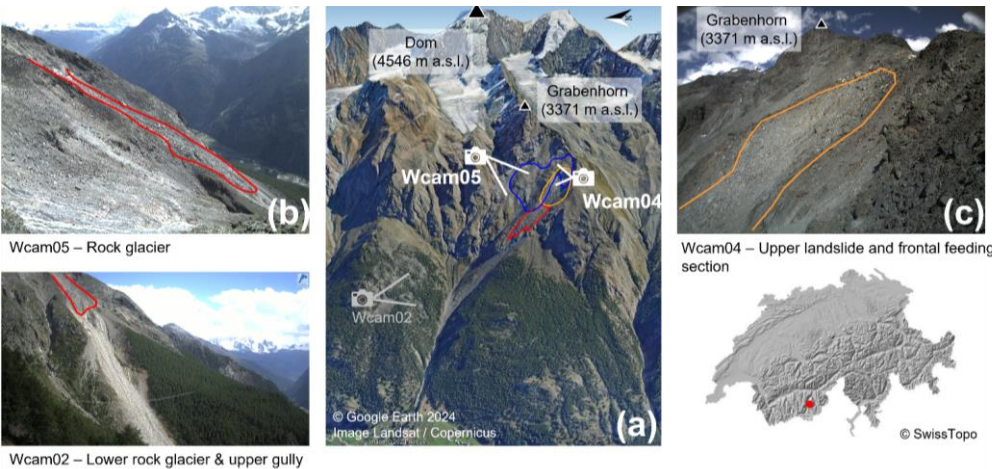
Figure 1: a) Overview of the Grabengufer study area in ~~the~~ Mattertal, Swiss Alps ~~with~~**, showing the locations of the webcams used in this study and the studied landforms (blue – landslide extent, orange – feeding section, red – rock glacier), b)** ~~an~~ **Example image from webcam Wcam05, capturing the rock glacier, and c)** example image ~~of the~~**from** webcam ~~(Wcam05) directed at a rock glacier and c) an example image~~**Wcam04, focused on the frontal section** of the ~~webcam (Wcam04) directed at the upper~~ landslide ~~area, used~~**feeding into the rock glacier—referred to as the feeding section** in this study.

~~The webcam characteristics are detailed in Table 1. The data used in this study was acquired by two Mobotix (M12, M15) webcams, each powered by a solar panel. The webcams capture images at hourly intervals during daylight conditions with a~~

170 resolution of 3.15 megapixels (2048 x 1536 pixels). The images are sent via a GSM (Global System for Mobile Communication) internet connection to a server for storage and accessibility. For scaling the acquired images, we make use of a high-resolution point cloud (4.89 cm/px, 419 points/m²), derived from an UAV flight performed on August 3, 2023 with a DJI Phantom 4 RTK at a flight height of 70 m above the terrain and subsequently processed in Agisoft Metashape Four ground control points were used as check points, demonstrating a planar accuracy of 1 cm and a height accuracy of 0.3 cm. For the

175 validation of the velocities derived from the time-lapse image sequence, we make use of bi-annual dGNSS surveys using real-time kinematics (RTK) collected at the beginning (30.06) and end (13.10) of the summer of 2022 and monthly theodolite measurements of fixed reflectors. Moreover, one fixed GNSS system installed on a large boulder within the landslide area (Glaciorisk) could be used to get higher temporal validation data of one point.

180

Table 1: Test datasets used in this study, as a selection of the entire datasets

185 The 3D reference data utilised for image-to-geometry registration was derived from UAV parallel-axis image flights conducted using a DJI Phantom 4 RTK. These flights were performed on July 3, 2023, and July 22, 2023, to reference images from Wcam04 and Wcam05, respectively. The image blocks were processed using Structure-from-Motion (SfM) techniques implemented in Agisoft Metashape v.1.7, resulting in high-resolution 3D point clouds enriched with RGB colour information. The georeferencing of these 3D point clouds employed an integrated approach, combining RTK measurements of image poses

190 and onboard IMU data. Additional ground control points (GCPs) were used to ensure a stable configuration (e.g., Elias et al., 2024). The dataset from July 3, 2023, comprises over 1,000 images captured at a constant flight altitude of approximately 85 m above ground level, yielding a ground sampling distance (GSD) of 2.5 cm/pixel. The overall reprojection error for the sparse points was 0.3 pixels. Four GCPs were incorporated for integrated georeferencing; however, the challenging terrain limited the inclusion of additional checkpoints. Positional errors at the GCPs were observed to be 1 cm in both horizontal and vertical

195 directions. It is important to interpret these errors cautiously, as they represent internal precision errors tied to the SfM-based 3D point cloud computation process. The dataset from July 22, 2023, covers an extensive area extending from the investigation site to the valley. Approximately 1,800 images were collected at a consistent flight altitude of around 88 m above ground level, resulting in a GSD comparable to that of the earlier dataset. Seven GCPs were strategically distributed across the area, from the valley floor to the upper slopes. Additionally, two independent checkpoints were established: one within the Wcam05

200 investigation area and another in the valley. The average residual error at the GCPs was approximately 4 cm in both horizontal and vertical components. However, deviations at the independent checkpoints were notably higher, with errors of 7.5 cm

horizontally and 9.5 cm vertically. Both 3D point clouds were resampled to a point spacing of 5 cm. This resampling facilitated the management of the large volume of 3D data, comprising hundreds of millions of points, while preserving detailed topographic representation. For further analysis, the point clouds were utilised to transfer the image measurements from the webcam to object space.

Table 1: Camera and image dataset specifications

Camera specs			Wcam04	Wcam05
		Camera model	Mobotix M12	Mobotix M15
		Sensor / pixel size (ps)	½" CMOS (6.4x4.8 mm) / 3.1μm	
		Image resolution	2048 x 1536 px (3.15 MPx)	
		Focal length (f)	5.4 mm (43 mm in 35-mm equivalent), crop factor 8	
		Viewing direction		
Wcam04 – Landslide / Camera pose		Location in CH1903+*	X: 2628628 m, Y: 1104523 m, Z: 2790 m a.s.l.	X: 2629114 m, Y: 1105319 m, Z: 2870 m a.s.l.
		Distance to landform	100 - 350 m	700 – 1,100 m

	View direction (NESW)	100 °	235 °
	Date of installation	01.09.2013	17.01.2011
	Sampling interval	hourly during daylight	
	Data transmission	GSM (Global System for Mobile Communication) internet connection (server storage)	
	# of images (start-2023)	48 118	51 919
Wcam05 Rock glacier	x: 700 17. f: 1.3 51 2629 01. mm 919 114, 201 235° y: 1 1105 319, z: 2870 m a.s.l.Subsample for study	Weekly images for summer 2022 (06.06 to 10.10.2022, 19 images)	

*CH1903+ is a commonly used Swiss coordinate system

3. Methods

210 The overall analysis was conducted step by step with the goalworkflow, visualised in Figure 2, consists of: several sequential steps designed to efficiently and accurately derive 3D trajectories from time-lapse image sequences. First (1) getting the), translation vectors or(pixel-based) trajectories (in pixels) from) for predefined tracking points to be tracked (, either arranged on a regular grid or at specified pixel coordinates), are extracted from the time-lapse image sequence in a fast and robust way (section 3.1), and 2) scaling. In the next step (2), these 2D trajectories from pixel coordinates, estimated between consecutive

215 images, are mapped to real-world coordinates using a 3D point cloud of the region of interest, which serves as the reference system (see Fig. 2). This transformation enables the calculation of 3D coordinates for the tracked points to calculategenerate 3D trajectories. Finally, these trajectories are used to compute velocities (in m per day) (section 3.2). Both steps apply existing AI frameworks and have limited , with units determined by the temporal resolution of the input requirements, reducing pre-processing time. Input of step 1data, such as the time-lapse interval (e.g., $m\ d^{-1}$).

220 Our workflow requires minimal input data. The primary requirement is a set of time-lapse images captured at a fixed time intervalintervals (e.g., weeklyhourly, daily, or hourly) withweekly), preferably awith datetime stampinformation embedded in

the ~~filename~~filenames. Additionally, approximate values for the camera pose and intrinsic parameters, such as focal length and pixel size, are necessary. No pre-filtering ~~of~~ to remove images affected by fog, snow, or motion blur is ~~required and there is no need for the prior stabilisation of the sequence to account for camera movements as the camera orientation parameters are to be calculated in the registration of image and object data. This requires a high-resolution 3D point cloud with RGB information of the area of interests and initial estimates of the camera's intrinsic parameters, i.e., focal length, as well as the camera pose, i.e., position and rotation in object space (Fig. 2). Given the short duration of this pilot study, we assume the cameras remain stable over time.~~needed.
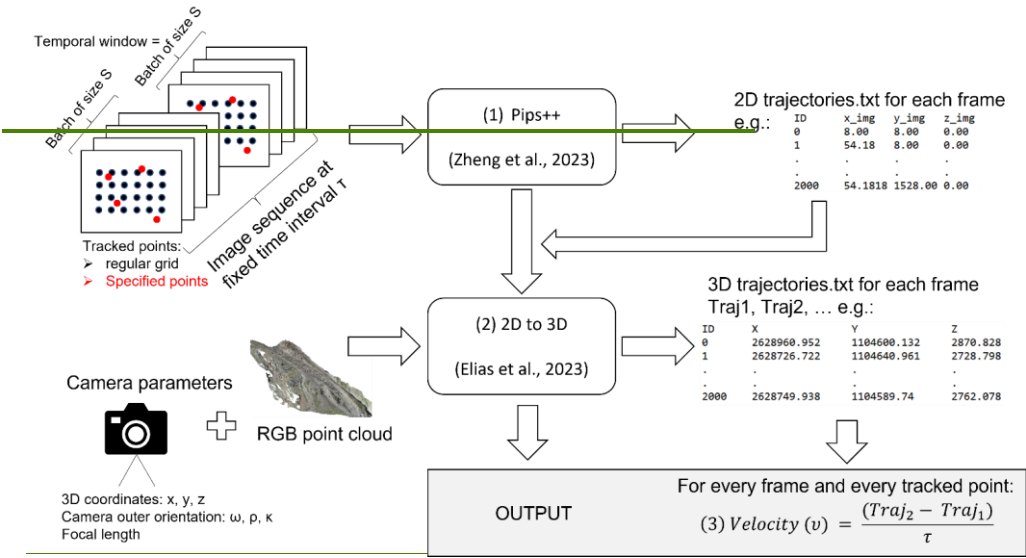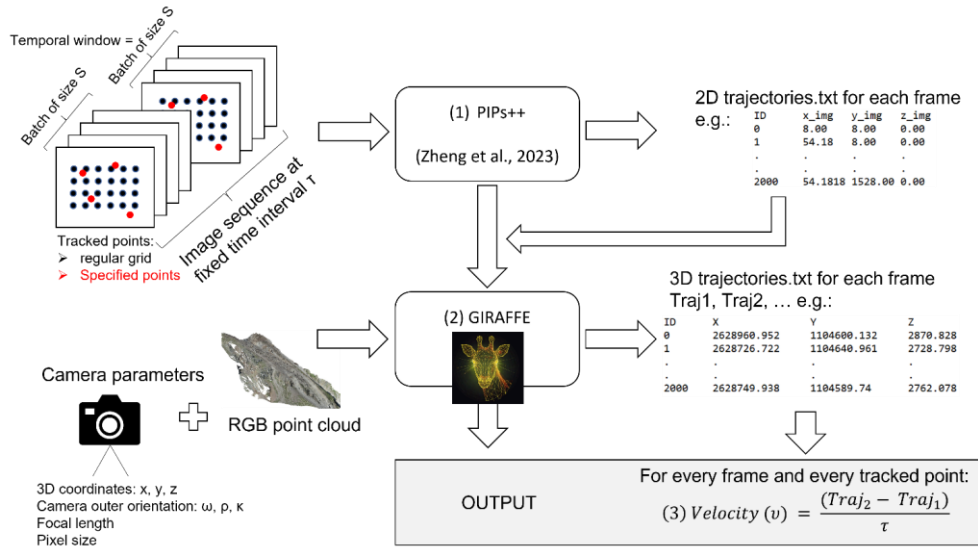
Figure 2: Schematic overview of the workflow presented in this study.

3.1 Application of the Persistent Independent Particle tracker (PIPs++)

The first step in our workflow ~~(Fig. 2)~~ involves feeding the image sequence, ~~taken at fixed time intervals (e.g., weekly, daily, or hourly),~~ into the Persistent Independent Particle tracker (PIPs++). This AI-based tracker, developed by Harley et al. (2022) and improved by Zheng et al. (2023), operates without retraining on our specific data. PIPs++ operates as a low-level tracker, relying on appearance-matching cues just like traditional methods, ~~and~~but leveraging the full information that is available from the image sequence within the temporal ~~priors~~window. It employs a 2D residual ~~Convolutional Neural Network~~ (CNN) for feature extraction in the initial step (He et al., 2016), generating a feature map for each frame~~,~~ independent of ~~temporal prior.~~the image before or after. Following feature extraction, the algorithm feeds into a deep 1D ~~Convolutional Network~~CNN (ResNet) with fixed-length kernels applied to arbitrary temporal spans (Zheng et al., 2023). ~~Based on the feature maps,~~ PIPs++ first detects features and then calculates descriptors to estimate the local similarity ~~and position of the features in an iterative step using~~of each feature to match them over time. Using spatial pyramids, it iteratively refines the position of these matched features, similar to the RAFT model (Teed and Deng, 2020). ~~Just like traditional methods, correlation~~Correlation matrices are calculated to ~~match~~align the feature templates. ~~The main difference from traditional methods is that this approach~~ as in already established approaches. PIPs++ operates within a multi-frame temporal context, considering all frames in a temporal window

or batch of size S to search for the target. After a match is found, the trajectory of the feature within the batch is updated ~~and new~~with one position per frame, resulting in a single, continuous trajectory per batch for that feature. The correlation ~~pyramids~~matrices are ~~calculated in an iterative way.~~recalculated iteratively to refine the tracking process. If tracking fails ~~for~~in

250 one frame due to occlusion (e.g., fog), the trajectory of the feature can still be estimated ~~as long as it is found in other~~by interpolating the position, provided that the feature reappears in subsequent frames within the batch (as long as the fog does not last longer than the batch size S~~) (; see~~ Fig. ~~3 B). Moreover, the~~3b). To increase robustness, the model computes similarity ~~is computed~~ using multiple templates per feature. This means that the model does not only rely on the feature's initial appearance ~~of the target~~ in the first frame, but ~~also on its~~adapts to changes in appearance along the trajectory, i.e., throughout

255 the sequence. ~~For each additional template, new correlations are computed and if tracking is successful it is included in the~~ If the feature's appearance changes, due to snow cover (Fig. 3d), lighting shifts, or rotation, the model can update templates along the trajectory, storing multiple representations (templates) for the same feature. This multi-template ~~tracking. This~~approach allows ~~for tracking the same features despite changes in~~tracking to continue even with appearance variations caused by environmental factors like light ~~conditions~~changes, snow cover ~~(Fig. 3 D),~~. or self-occlusion (e.g., rolling boulders~~), by~~

260 ~~handling). Thus, the model handles~~ appearance changes flexibly and ~~considering the trajectory to extract~~tracks the feature over time using these multiple templates ~~per feature~~. For further information about the model architecture, we refer to Harley et al~~.,~~. (2022) and Zheng et al~~.,~~. (2023). The output of the model is a simple trajectory .txt file per frame (see Fig. 2, lower right), with the pixel coordinates of each tracked point. This file can be visualized on the respective image for visual inspection (Fig. 3). If a regular grid is used, it is reset each time a new batch starts. ~~When camera movements occur, a homogeneous and mono-~~

265 ~~directional translation or shift of the regular grid in the stable areas can be observed (Fig. 3C). This shift can be corrected by applying a simple adjustment based on its vertical and horizontal components, similar to the method used by Kenner et al. (2018).~~
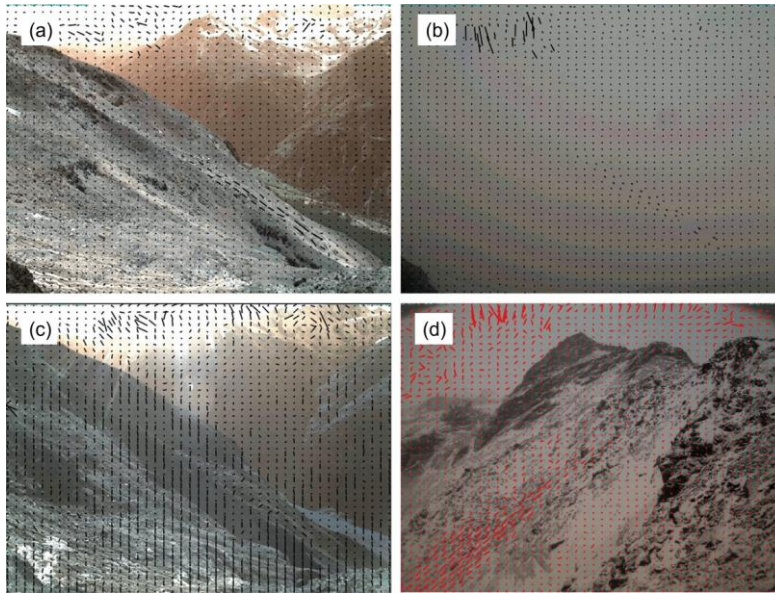
Figure 3: Some examples of velocity vectors as output from the PIPs++ model, a) view of Wcam05, clearly identifying the moving rock glacier body although its suboptimal viewing angle, b) same view occluded by fog but tracking is interfered from the ~~temporal prior~~image before and after, c) same view displaying a systematic shift in the stable areas due to camera movement, d) view of Wcam04 proving PIPs++ good performance in varying snow conditions.

~~Depending on computational power and image resolution (in our case 3MP), a certain number of points (N) can be tracked within a certain batch size (S). In our case, we used an NVIDIA RTX A6000 GPU, with 48 GB of memory and were able to track 2000 points in a batch size of 19 frames. This means that for a temporal window of 19 frames, the same 2000 particles are tracked before resetting the grid and starting anew. Processing 400 images in this set up took around 2 minutes. For validation, specified points, such as boulders with available GNSS data, can be tracked in addition to the grid points entered into PIPs++, demonstrating the system's accuracy and reliability. These points are inserted in the script as pixel coordinates.~~

3.2 From 2D to 3D: image-to-geometry ~~scaling~~registration using GIRAFFE

~~The second step in the workflow (Fig. 2) is based on the methodology first introduced in Elias et al. 2019 and later updated in Elias et al. 2023. The approach is called image-to-geometry registration and enables the transformation from 2D image data into 3D object space by matching a camera image to a synthetic image rendered from a coloured 3D point cloud preserving~~

285 ~~location and depth information. This synthetic image should match the image geometry of the real camera as much as possible, which is why an initial guess on the true camera pose, i.e., position and viewing direction, as well as the cameras focal length and pixel size are required for synthetic image rendering. The 2D-3D matches are used to perform space resection to determine the camera pose and, assumed well-distributed key points in view of the camera image, cameras intrinsic parameters and lens distortion (Fig. 4). For matching camera and synthetic image, image-to-geometry registration was adapted using the AI-based~~
290 ~~matching approach LightGlue (Lindenberger et al., 2023). LightGlue is a high-performance, open-source adaptation of SuperGlue (Sarlin et al., 2020) and is excellent for registering images to each other, even if they differ greatly in geometry and radiometry. After determining the camera pose and internal camera geometry in the reference system of the 3D point cloud, image information can be mapped in 3D space by back projection (called "scaling"). Initial camera properties of the used time-lapse cameras (Table 1) are available and we can access the detailed topography of the scene through a single UAV~~
295 ~~measurement, described above.~~

Image-to-geometry registration, implemented in GIRAFFE, transfers 2D image data into 3D object space by aligning the camera image with a photorealistic synthetic image. This synthetic image is rendered from a coloured 3D point cloud using an initial estimate of the camera's original pose within the point cloud's 3D object coordinate system. The user must provide an approximation of the focal length and the pixel size of the actual camera. The synthetic image will replicate the camera
300 perspective of the real camera image while preserving the spatial information from the 3D point cloud. Note, the colour information could also be inferred from intensity values, e.g., from a TLS/ALS point cloud, particularly when significant differences in intensity arise due to the varying reflectance properties of topographical features. However, in natural settings, such as the Grabengufer site, the intensity images typically lack sufficient unique features to facilitate alignment with camera images. Therefore, we utilise RGB-coloured 3D point clouds derived from UAV photogrammetry.
305 The rendering process involves projecting the 3D points of the point cloud onto a virtual image plane, assuming a linear pinhole camera model and accounting for gaps and occlusions. Points closer to the camera contribute more information to the virtual image plane and are less likely to be occluded by other points along the depth direction. The view frustum is determined using a method known as frustum culling (illustrated in Fig. 4). Despite variations in point size, gaps remain in the projected point cloud image. These gaps are addressed using a radiometric gap-filling algorithm based on a k-nearest neighbour (kNN)
310 approach. Although the pixels generated through gap filling do not correspond to actual 3D information, they assist the matching algorithm in subsequent steps by facilitating correspondences between the real and synthetic image.

Once the synthetic image is generated, it provides a photorealistic depiction of the 3D point cloud matching approximately the perspective of the original true camera image, retaining the original 3D information (except in areas filled radiometrically by the gap-filling process). Using LightGlue, homologous points between the real and synthetic image are identified and matched,
315 resulting in a list of corresponding 2D-3D image coordinates. A kNN approach is applied again to the synthetic image to find the nearest neighbour for each image coordinate from the list that corresponds to a valid 3D point. By default, a maximum distance criterion of 2.5 pixels is employed. This process produces a dataset of 2D image measurements from the real camera image, corresponding to 3D object points from the synthetic image.

These matched 3D object points can be treated as pseudo-control points to solve the camera pose, principal point location, and principal distance using an extended space resection approach formulated as a perspective-n-pose (PnP) problem. We employ the pinhole camera model and Levenberg-Marquardt optimisation implemented in OpenCV v4.10. When the distribution of 2D-3D point correspondences is uniform across the image (and sufficiently high to solve for more unknowns), this approach can also estimate lens distortion parameters. If the distribution is not suitable, lens distortion is neglected, which might lead to inaccuracies in referencing image measurements, particularly at the image margin. Pre-calibration of the camera may be performed because then images can be undistorted based on the calibrated interior orientation parameters before further processing in PIPs++. After determining the camera model of the real image - either linear (without distortion parameters) or non-linear (with distortion parameters) - including the intrinsic parameters and camera pose within the reference system of the 3D point cloud, a connection is established between 3D points in the synthetic image and corresponding 2D points in the aligned real image. This connection can be used to identify discrete 3D coordinates for specific image measurements or to transfer thematic information from the image to the 3D points in the synthetic image, enabling additional data to be applied to the 3D point cloud for mapping purposes. This process can be considered a simplified form of back-projection.

The accuracy of the computed camera model, and consequently the precision of the 3D-referenced image points, is governed by two primary factors: the accuracy and density of the 3D point cloud, which serves as the source of pseudo GCPs for space resection, and the spatial distribution of corresponding image observations, particularly when estimating the parameters of a non-linear camera model. To address this, we implemented an automatic distribution control mechanism, ensuring that the determination of the non-linear camera model is performed only if the pseudo-control point configuration meets the requirement of an adequate spatial distribution (i.e., points well-distributed across the entire image, including the edge regions). To achieve stable results for the exterior orientation parameters, the pseudo-control points must also be well-distributed in object space and should avoid collinear alignments or geometrically degenerate configurations, such as cylindrical or conical surfaces. In practice, when utilising a pseudo-control point field derived from a naturally occurring topography with thousands of potential 3D control points, the likelihood of such problematic constellations is negligible. Additionally, the distance criterion used to assign a 3D point to a 2D match with the real image in the synthetic image plays a critical role in the accuracy of the 2D-3D association. A smaller distance threshold results in higher precision for individual matches; however, it also reduces the number of available pseudo-control points, potentially affecting the robustness of subsequent space resection steps. Striking an appropriate balance between precision and the density of control points is thus essential for optimising the overall calibration process.

GIRAFFE enables the iterative execution of image-to-geometry registration and space resection, allowing for the gradual refinement of the (non-)linear camera model. By default, the software is configured to perform three iterations, a value determined empirically as a balance between computational efficiency and the likelihood of achieving convergence even with suboptimal initial parameter estimates (one iteration takes between a few seconds and a minute, depending on the point number of the used 3D point cloud). With each iteration, the synthetic image generated by GIRAFFE increasingly aligns with the perspective of the real camera, improving both the number and spatial distribution of pseudo-control points. This iterative

approach enhances the stability and robustness of the camera model adjustment procedure while accommodating coarse initial guesses with higher reliability.
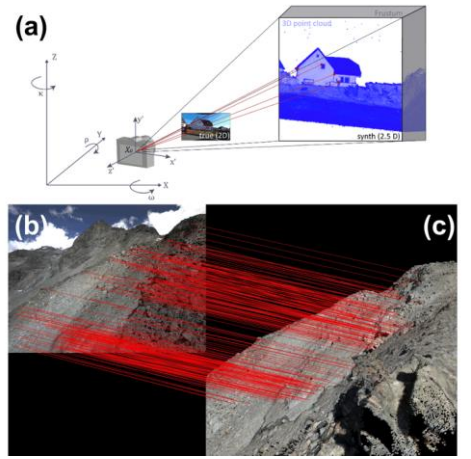
Figure 4: a) Visualisation of the image-to-geometry scaling (Elias et al., 2023), b) real 2D image from Wcam04 being matched to c) the rendered synthetic image derived from the UAV data, displaying a good distribution.

The accuracy of the determined camera calibration and thus the accuracy of the scaled 3D data is directly linked to the accuracy and quality of the 3D data. The point cloud data needs to include colour information to ensure matching to succeed. This information could either be RGB, which is common when originating from photogrammetry, or intensity information that could be used for colouring. Note, the use of 3D point clouds with intensity values from laser scanning in image-to-geometry registration requires objects that can be clearly distinguished from each other in the intensity image by different properties with regard to their reflectance. This is the case, for example, when used in urban areas where building features can be excellently distinguished in the intensity-coloured synthetic image due to different materials and consequent reflections (see Elias et al., 2023). In natural settings, like the Grabengufer site, the intensity-image will not provide enough unique features to be aligned with the camera image which is why we use an RGB-coloured 3D point cloud from UAV photogrammetry for scaling.

355

360

365

3.3 Combining PIPs++ and GIRAFFE

3.3.1 Image Pre-Processing

We assumed that the poses of both webcams remained stable over the 19-week observation period. However, we noticed slight movements of Wcam04 caused by wind, which we corrected using a homography-based transformation. Thereby, the first image of the time-lapse sequence is considered the reference to which all subsequent images are registered using SIFT to estimate the points for homography calculation. This calculation is done using the RANdom SAmple Consensus (RANSAC) method to account for potential outliers, such as moving image features in the area of the rock glacier or landslide, which could otherwise introduce errors. The derived homography is then applied to perform a projective transformation of all consecutive images. In this way, the camera model could be considered consistent for all images of the analysed time-lapse sequence. Accordingly, we employed GIRAFFE only to the reference image to ascertain the configuration of the image geometry and utilised the estimated camera model to reference all pixels tracked by PIPs++ throughout the sequence in object space.
In contrast to this image-based stabilisation, the camera model of each image of the time-lapse sequence could also have been calculated independently of the others via GIRAFFE and applied to the respective PIPs++ image measurements. However, this method was not employed due to the superior robustness of image-based stabilisation, particularly under poor image quality conditions, such as those caused by fog. Note that this type of image pre-processing is only necessary if the camera's extrinsic geometry appears to change. Otherwise, AI-based feature tracking can proceed directly from the initial images.

3.3.2 Image feature tracking and 3D referencing

We used a NVIDIA RTX A6000 GPU with 48 GB of memory to track 2000 points across a batch size of 19 frames on 3MPx-large images before hitting computational limits. For a temporal window of 19 frames, the same 2000 features are tracked continuously before the grid was reset, after which tracking restarted with the reset grid as new input. Processing 400 images with this setup took approx. two minutes. For validation, specific points of interest, such as boulders with available GNSS/TS data, were tracked in addition to the grid points entered into PIPs++. These specific points were inserted into the script as pixel coordinates.
Initial camera specifications for the time-lapse webcams were available from EXIF metadata (i.e., focal length) and GNSS-measurements of the camera housings, which was used as approximation for the 3D coordinates of the camera projection centres. It is assumed that the camera is not tiled or rotated along the lateral axes of the reference system. The viewing angle related to the geographic view direction (NESW) was determined by compass. The pitch and roll angles were assumed to be 90 degrees (looking parallel to the XY-plane) and zero degrees (no rotation around the viewing axis). Although our initial estimates for the camera model from GNSS, compass and image EXIF data were already sufficient, we used three iterations during the optimisation. The image points tracked by PIPs++ were referenced registering the reference image of the time lapse sequence to the 3D object space. The camera distortion coefficients could not be determined due to unsuitable distribution of

pseudo-control point observations as large portions of the image were covered by sky and topography not represented in the 3D UAV data.

The resulting lists of 3D coordinates per timestamp matched the PIPs++ feature points and were accompanied by an identifier that allowed the 3D coordinates to be uniquely assigned across the timestamps to estimate the per-camera 3D trajectories. 405 Finally, mean velocities in metres per day were calculated dividing the displacement between two consecutive 3D points by the time interval, resulting in a total of 18 velocity measures per tracked image point.

4. Results

4.1 Geomorphic results

Our image-based 3D trajectory and velocity measurements were based on two subsets from time-lapse cameras perspective. 410 As a rule of thumb, the more similar the perspectives of camera and synthetic image, the more matches are likely to be found and the better the parameters of the pose and interior camera geometry of the camera image can be determined and used for scaling the image information. In this study, we parametrized image-to-geometry registration in a way, that three iterations are performed. Details on parameters are given in Elias et al. (2019) and Elias et al. (2023).

After the results are scaled, absolute distances and velocities are calculated for each tracked point (Fig. 2 (3)), within the chosen 415 time interval, in this case every week for the summer of 2022. A spatial aggregation is performed to split the results for the active moving part (the landslide or the rock glacier) and the points in the presumed stable area. An accuracy analyses is performed on the points in the stable areas, where the calculated velocities are expected to be close to zero.

4. Results and validation

As a pilot study, we processed a small subset of two time-lapse image datasets (Table 1), of of a permafrost-affected landslide 420 and its frontal section feeding into a rock glacier, with the workflow outlined above.. The results for both areasinvestigated region of interests for the entire summer period (06.06 to. until 10.10.2022, 19 weekly images) are shown in Figure 5 A.

The results are coherent with what we expect 5a. As expected from the landform displacements, showingthe results show a largely homogenous flow velocity flow field with faster velocities in the upper area of the rock glacier and in the scarp area of the landslidefeeding area of the landslide., Points in blue display stable areas for the considered timeframe of 127 days. Especially in the landslide area, there are single large boulders that move faster than their surroundings. For validation, measured fixed, dGNSS and theodolite data were used, acquired at the beginning and end of the summer season. Unfortunately, not all measured points were suitable for validation because they were not in direct view of the camera and thus could not be included. Additionally, in the fast-moving areas, no dGNSS points could be measured due to logistical and safety constraints (Fig. 5B). As a result, only a few velocities derived from theodolite measurements could validate the higher velocities observed in the time-lapse sequence (Fig. 5A). More interestingly, validation was also conducted by examining detected motion in presumed stable areas (Fig. 5C). Here, we observed a clear abundance of points around zero, as expected for stable areas, with noise of about 1 cm/day. When considering weekly images, our method and camera setup can thus detect real movement if it surpasses 7 cm. An average landslide movement of 0.03 m d⁻¹ (0.21 m of absolute movement of 4 cm per day (28 cm per week) was

derivedbetween weekly images) was observed across the entire feeding section, while in stable areas, detected movement was mostlytypically below 4 cm per day (Fig. 5C). In more detailed observations of the0.01 m d⁻¹ (Fig. 5c). For the rock glacier, the average movement during the summer period was 0.10 m d⁻¹ (0.21 m of absolute movement between weekly velocities of

445 the landslide (Wcam04), we notedimages), with stable areas showing movement generally below 0.05 m d⁻¹. The feeding section exhibits significant spatial variability, with certain large boulders moving faster than their surroundings, unlike the rock glacier, where movement is more uniform. This variability must be considered when using discrete points from GNSS and TS measurements to characterize landform movement. While the two TS points used to validate the Wcam05 velocity estimates show a similar trend to the overall movement of the rock glacier using (Fig. 7b), the permanent GNSS system reveals

450 a distinct peakmovement pattern, with a marked acceleration in velocity inat the second halfend of July (Fig. 6). These observations align with the measured velocities from a fixed GNSS device installed on a large boulder (Fig. 5, red location pin).that is not reflected in the feeding section's overall movement (Fig. 7a).

The uppermost landslide area and the lower rock glacier are presumably driven primarily by permafrost creep. However, the driving mechanisms of the frontal feeding section observed by Wcam04 remain unknown. To better understand the factors

455 controlling factors of these velocity changes and to ultimately improve our understanding of landform the overall behaviour of these landforms, further investigation ofinto environmental drivers such as rainfall and temperature is required.necessary – especially considering that the summer of 2022 was exceptionally warm and dry, with consecutive heat waves. However, this is beyond the scope of the current pilotthis study.

460
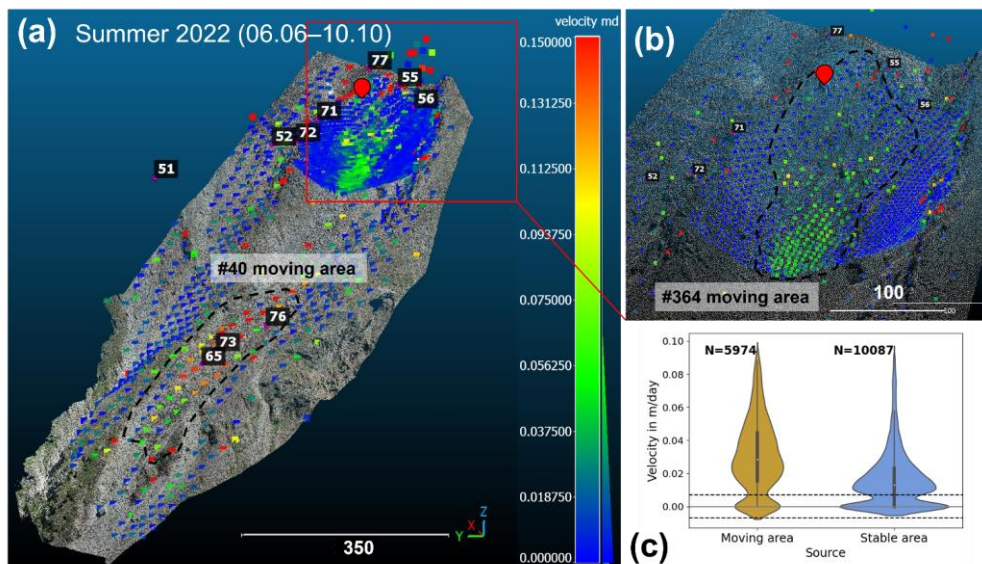
Figure 5: a) Velocity results (in m d^{-1}) over the entire summer period (127 days) for both the feeding section (upper area, observed by Wcam04) and the rock glacier (lower area, observed by Wcam05), displayed on UAV point cloud data, including total station-measured points (black and white labels) and the permanent GNSS installation (marked with a red location pin), b) close-up of the frontal feeding section (Wcam04), c) plot of the weekly velocity distribution for both the moving and the stable areas (data from Wcam04), showing a clear noise level between ±0.007 m d^{-1} in both regions. Dotted lines indicate the moving areas in this study. Points in blue display stable areas for the considered timeframe of 127 days.
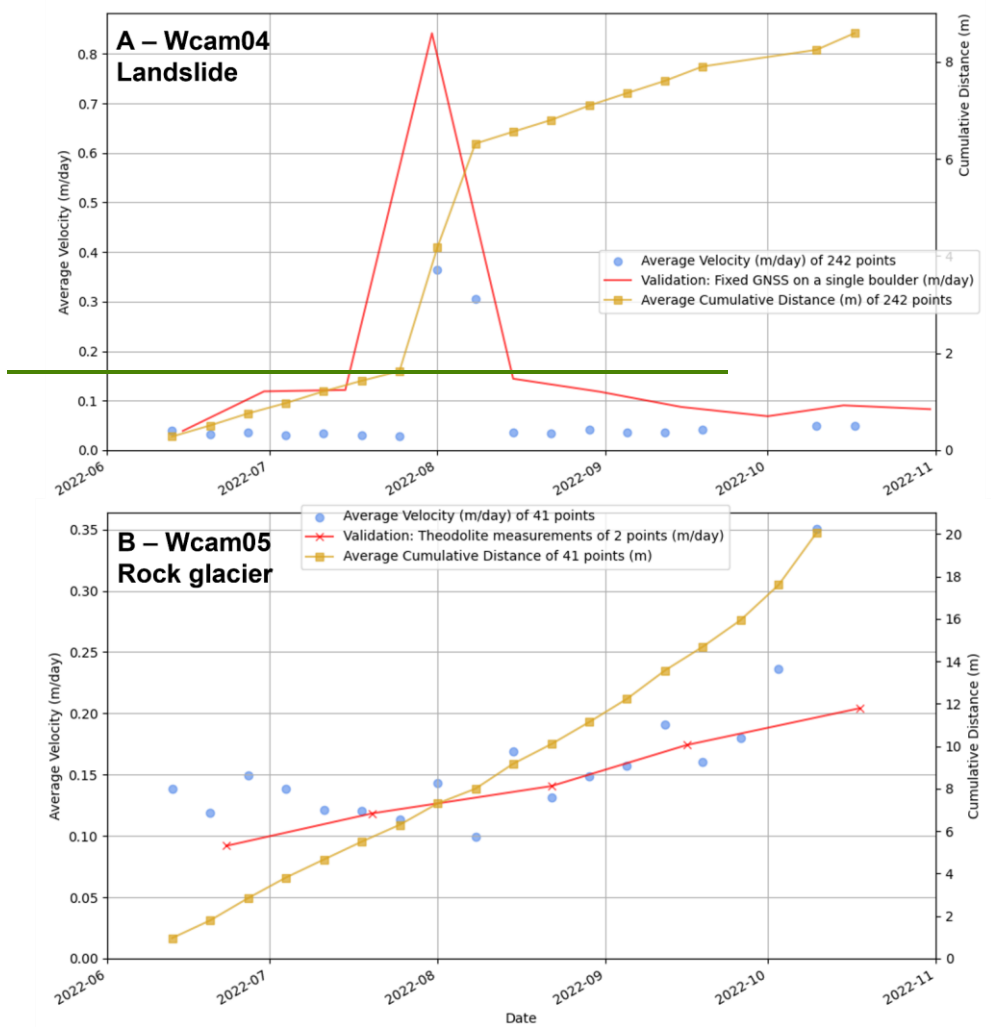
Figure 6: Graph with

4.2 Error Assessment and Validation

The accuracy of the 3D trajectories and velocity derivations essentially depends on three factors: The reliability of the PIPs++ feature tracking, the determination of the camera model by image-to-geometry registration, and the resolution and accuracy of the 3D point cloud. To assess the accuracy potential, a comprehensive analysis of all potential sources of error was necessary. However, due to the numerous algorithms, a classic error analysis is difficult, especially because AI-based tools such as PIPs++ often do not provide any information on reliability. We have included the following methods in our evaluations:

- Level of Detection (LoD): Assessing pseudo-movements in stable areas resulting from an accumulated error of PIPs++ measurements and its translation into object space define a so-called LoD, describing the threshold of significant movements that could be detected with our method.
- Theoretical accuracy analysis based on the reprojection results of GIRAFFE.
- Validation with ground truth data by comparing our measured 3D trajectories with GNSS and TS data at selected 3D objects.

4.2.1 Level of Detection

The LoD was experimentally determined analysing the detected 3D movements in presumably stable areas (Fig. 5c). For Wcam04, the designated stable area lies within the broader zone of the deep-seated landslide (Fig. 1a, blue polygon). While this area moves significantly slower than the frontal feeding section, its stability is relative and only valid when considered over a short timeframe. Here we detected a LoD of about 0.007 m d^{-1} or an absolute movement of 5 cm between weekly time-lapse images. For Wcam05, the LoD was around 0.02 m d^{-1} or an absolute movement of 14 cm between weekly image frames, which is consistent with the larger camera-to-object distance (Table 1).

4.2.2 Theoretical accuracy analysis

For both the stable (Wcam05) and software-stabilised (Wcam04) time-lapse image series, the GIRAFFE software was employed once to estimate the linear camera model of the reference image. To assess the precision of the image-to-geometry registration, GIRAFFE calculates the overall root mean square error (RMSE). This is achieved by projecting the 3D pseudo-control points used for space resection back into the image using the estimated camera model and measuring the mean distances between the original image observations and their projected positions. The RMSE for Wcam04 and Wcam05 was 4.8 pixels and 4.5 pixels, respectively.

Based on the initial parameters of Wcam04 and Wcam05, we perform a theoretical accuracy analysis considering the RMSE values. For Wcam04, the camera-to-object distance ranges between 100 m and 350 m, resulting in an image scale ranging from 1:18,000 to 1:65,000. An error of 4.8 pixels in the image corresponds, given a webcam pixel pitch of 3.1 µm, to a positional error in object space between 0.3 cm and 1.0 m, respectively. In contrast, for Wcam05, the camera-to-object distance is between 700 m and 1,100 m, leading to a varying image scale of 1:130,000 to 1:200,000. Under the same pixel size assumption, a 4.5-

500 pixel error translates to an object space error of 1.8 m to 2.8 m, respectively. These results highlight that as the camera distance increases, minor uncertainties in camera geometry modelling can lead to significant errors in the measurements in object space. Consequently, higher inaccuracies are expected for Wcam05.

To mitigate errors resulting from the estimated camera model, particularly at smaller scales, GIRAFFE by default applies an outlier filtering of the registered image measurements in object space. Only 3D coordinates with a reprojection error below
505 2.0 pixels were retained to ensure the inclusion of features reliably located in the 3D object space based on the estimated camera model. A translation of the maximum permitted reprojection error of 2.0 pixels into object space reveals the maximum expected error of the 3D points, providing the base of the 3D trajectories, which varies in accordance with the image scale, i.e. between 0.10 m and 0.40 m for Wcam04 and 1.0 m and 1.2 m for Wcam05.

4.2.3 Validation with ground truth data

510 To validate our method with ground truth data from GNSS and TS, we selected individual 3D objects visible in the camera's field of view and excluding those with movements close to or below the LoD. Due to logistical and safety constraints, the ground truth data does not cover the fast-moving areas of the frontal feeding section. However, they are available in the upper landslide area (Fig. 5b). At least, two moving objects were suitable for direct validation, both located on the rock glacier observed by Wcam05. And for Wcam04 one permanently installed GNSS antenna in the view was available for validation.
515 However, no further objects were available because the GNSS and TS data was outside the camera's field of view or the image-based results were below the LoD. For the two object points visible in Wcam05, 3D trajectories across five timestamps were reconstructed, resulting in eight measurements suitable to validate the 3D trajectories measurements from PIPs++ and GIRAFFE. Given the challenge of precisely identifying the measured ground truth point in the image data, we tracked 5x5 patches around the presumably image position of the respective object, i.e. 25 pixels (Fig. 6a).
520 We fitted 3D lines as trajectories instead of using individual 3D points for validation because this offers the advantage that we can reduce the impact of noise and outliers in the data to investigate systematic errors. Thereby, we need to assume a linear movement, which however was apparent from the reference data provided by TS. The standard deviation of the perpendicular distances between the points and the fitted 3D line was calculated. These distances quantify how well the points align with the fitted line for both the reference measurements and the PIPs++/GIRAFFE measurements. The measurements from
525 PIPs++/GIRAFFE for Wcam05 (Fig. 6b) exhibit a considerably higher level of noise compared to those from the TS (Fig. 6c,d). However, if we consider the spatial (XYZ) differences of the vectors and the Euclidean distance between the vectors, we see that the total discrepancy of the directions and thus of the approximated 3D trajectories in 3D space is of the order of only a few decimetres. We conclude that the measured 3D trajectories obtained using PIPs++ and image-to-geometry registration are subject to random fluctuations, ruling out the presence of systematic errors. Furthermore, the directional
530 differences between reference trajectories and our measurements indicate a variation of a few degrees (Table 2). These discrepancies are largely attributable to the difficult image-to-object imaging configuration and the resulting difficult grinding cut geometries.

For Wcam04, the points exhibited minimal movement during the observation period, which limited the ability to fit straight lines to the 3D trajectories. However, the basic distance between the reference and image measurements was determined using the centre of gravity of the respective 3D point sets. This approach enabled an estimation of the general accuracy of fit based on the 3D coordinates. A relatively large offset of 1.3 m was observed (Table 2), attributed to the GNSS antenna being positioned behind a boulder and therefore not visible in the image. Consequently, we had to track the opposite side of the boulder for validation instead of the antenna's actual position. Given that the boulder is approximately the size of a small car, this offset is likely due to the discrepancy in tracked position. However, the same velocity pattern could be observed in both the GNSS data and the tracked point in PIPs++/GIRAFFE, though to a minor extent (Fig. 7).

Table 2. Calculation of fitted 3D trajectories of significant objects tracked over 109 days with GNSS (one point, visible in Wcam04) and over 118 days with TS (two points, visible in Wcam05) as well as with PIPs++ and GIRAFFE in the associated images, taken on the same days as the GNSS/TS ground truth measurements.

ID	Date	SD line fit GNSS/ TS [m]	SD line fit PIPs++ / GIRAFFE [m]	Diff X [m]	Diff. Y [m]	Diff. Z [m]	Diff total movement [m]	Diff direction [°]
TS_65	23/06/2022 20/07/2022 22/08/2022 16/09/2022 18/10/2022	0.08	0.29	0.14	0.19	0.05	0.25	14.38
TS_73	23/06/2022 20/07/2022 22/08/2022 16/09/2022 18/10/2022	0.05	0.59	-0.10	-0.09	-0.03	0.14	8.23
WCam05 - Absolute Mean Error (ME) [m]	**-**	**-**	**0.12**	**0.14**	**0.04**	**0.19**	**11.3**
GNSS	30/06/2022 15/07/2022 31/07/2022 15/08/2022 31/08/2022 15/09/2022 01/10/2022 15/10/2022 31/10/2022	-	-	0.86	-0.94	0.01	1.28	-
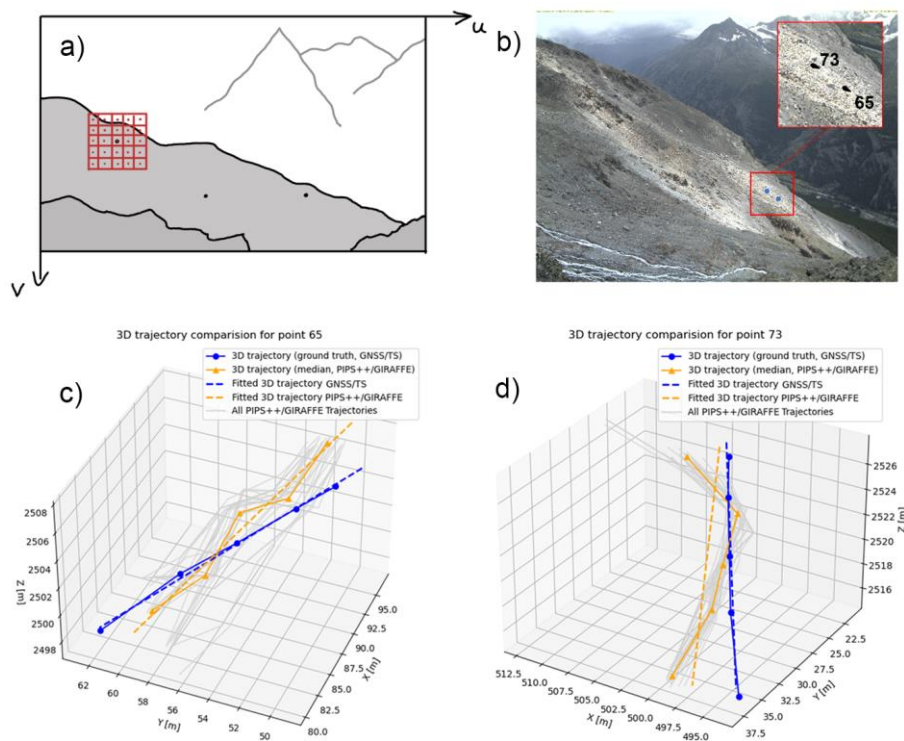
Figure 6: Validation through direct comparison of two measured point trajectories (ground truth) and their corresponding trajectories derived from time-lapse images. a) A 5x5 pixel grid around each ground truth point captures local movement. b) Location of the two validation points on the rock glacier observed by Wcam05. c) Trajectory of point 65: ground truth (blue), time-lapse-derived trajectory (median of 25 trajectories, orange), and individual trajectories from the 5x5 grid (grey) as well as the fitted 3D trajectories (dashed lines). d) Same data presented for point 73. For visualisation purposes, we applied an XY-offset in metres of [2.628*10^6, 1.105*10^6].
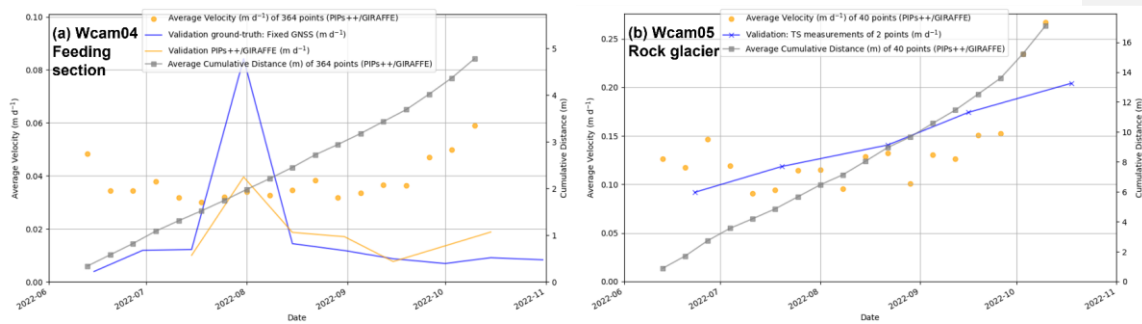
Figure 7: Graphs showing weekly velocities and cumulative ~~distance of~~distances. **Panel a) displays data for** the ~~landslide (A~~ ~~feeding section (~~Wcam04) **and** ~~panel b) for~~ the rock glacier (~~B~~Wcam05) ~~in~~during **the summer of 2022**, **derived from time-lapse imagery** ~~(note~~. Note **that** ~~the~~ **data** ~~of~~from **October** ~~26/10~~ **is** ~~not displayed for~~excluded from **graph** ~~A since this was~~ a~~) due to~~ **foggy** ~~image~~conditions **and was interpolated by the model)**. ~~The validation~~. Validation **points**, **marked in red** ~~is~~, **include measurements from the** ~~fixed~~permanent **GNSS installed on a** ~~single~~ **large boulder in the upper** ~~landslide~~feeding **area (**~~A~~a**) and** ~~of~~ **two theodolite points** ~~measured~~ **on the rock glacier (**~~B~~b**).**

~~4~~5**. Discussion**~~, limitations~~ **and** ~~outlook~~Limitations

~~4~~5.1 General performance of the proposed workflow

The above-described methodology has the potential to tackle entire time-lapse image datasets to determine landform velocities, in this case creeping permafrost landforms. The results of our workflow show a good agreement with ~~dGNSS,~~GNSS and TS theodolite ~~and fixed GNSS~~ measurements~~,~~ considering the low-grade camera's used (Table 2, Figure 6), proving our method to be reliable, robust and fast for creating a better spatial (Fig. 5) and temporal coverage (Fig. ~~6~~7) of the landform's displacement. Our pilot study demonstrates that significant ~~new~~motion and velocity information can be rapidly and easily extracted using AI-based methods from a basic ~~and~~, cost-effective device like a single webcam, greatly enhancing temporal acquisition frequency without the need for ~~an array of cameras. This approach reveals sub-seasonal patterns, such as the short-term acceleration observed in Figure 6, which reflects either actual motion related to permafrost creep or specific movements in the active layer, typically following significant water input from snowmelt or rain (RGIK, 2023). Spatial heterogeneity of landform movement (Fig. 5)~~a camera array. Spatial heterogeneity of landform movement is evident as well, including instances where larger boulders move faster, seemingly 'surfing' on the main landslide body. This phenomenon ~~is~~, illustrated in Figure ~~6, where fixed~~7, is supported by in-situ GNSS data, which indicates faster ~~overall~~ movement compared to the overall landform.

If this pattern were seen across the entire landform, albeit followingit could suggest motion linked to permafrost creep or specific movement in the active layer, often triggered by significant water input from snowmelt or rainfall (RGIK, 2023). However, the movement seems restricted to large boulders, possibly pointing to a similar temporal pattern. gravitational origin due to the steep terrain.

Although our proof-of-concept did not achieve the centimetre to millimetre accuracy of fixed GNSS and TS measurements, we were still able to detect absolute displacements of 75 cm and 14 cm between consecutive frames (in our case weekly) using the setups of Wcam04 and Wcam05, respectively (Table 1). The measurements at the rock glacier (Wcam05) have a significantly lower spatial resolution (4140 vs. 242364 points tracked onin the landslidefeeding area) due to the greater distance of the webcam from the area of interest and its suboptimal viewing angle (Fig. 1B1b). This increased distance also made the measurements more sensitive to slight camera movements, which, along with the lower level of detectionLoD, likely contributed to some of the higher variation in measured rock glacier velocity (Fig. 5B6b). The output of our workflow in a sense yields a sparse point cloud for every image frame in the sequence with absolute distance and velocity information as a scalar field, as visualised in Figure 5. This provides a great amount of spatial and temporal data in a manageable file format suitable for big data.

The superior performance of the PIPs++ model stems from tracking multiple timesteps jointly instead of frame-by-frame, enhancing temporal smoothness, coherency, and improving flow estimation accuracy (Hur and Roth, 2020). This makes PIPs++ especially suitable for environmental applications, where for example changes in light conditions are a common problem. Moreover, PIPs++ is trained on a very large and diverse artificial dataset PointOdyssey (Zheng et al., 2023), including rendered dynamic fog to account for (partial) occlusion and realistic in- and outdoor scenes. This entirely absent from other synthetic datasets like the FlyingChairs dataset, which was utilised to train models such as FlowFormer (Huang et al., 2022) or GMFlow (Xu et al., 2022), i.e. transformer-based models, and justifies our use of PIPs++ as a tracker in this proof-of-concept without the need of re-training the model with a sample of our own data. While previous research using monoscopic images to track a landslide (Travelletti et al., 2012) and a rock glacier (Kenner et al., 2018) was prone to mismatches because of its frame-by-frame strategy, our approach surpasses this limitation and at the same time makes it possible to process longer time periods and handle big data collected by hourly webcams more adequately. By also tracking points in stable areas, shifts in camera position, a common problem in long time-lapse imagery sequences, can be corrected and used for stabilising the image sequence, similar as in Kenner et al. (2018). A main limitation of the method developed in the latter research is the requirement that the creep directions and the geometry of the mass wasting area remains unchanged due to the use of fixed azimuths and masks for georeferencing. This is solved in our methodology, since PIPs++ does not assume any movement direction (Zheng et al., 2023) and no masks are needed when scaling the data using our image-to-geometry approach (Elias et al., 2023).By tracking points in stable areas using either hand-crafted point operators like SIFT or AI-based methods, shifts in camera position, a common problem in long time-lapse imagery sequences, can be corrected to some degree to stabilise the image sequence by software. When using PIPs++ and GIRAFFE, two options exist to deal with camera movements: a) image stabilisation by software or b) individual referencing of each time-lapse image, i.e. run GIRAFFE image-per-image. The

correction based on image pixels is frequently accomplished through the calculation of a homography to match a reference image. However, this method is only capable of compensating to a limited extent for perspective distortions resulting from changes in perspective due to camera movements. Consequently, it is most suitable for smaller movements. In cases of stronger movements, we recommend calculating the camera model individually for each individual image of the image sequence, whereby the relationship to the point cloud is calculated individually. As a result, even major changes in perspective should be handled adequately when translating the image measurement into object space.

5.2 Limitations

As PIPs++ still relies on appearance-matching cues ~~like~~similar to traditional methods, it ~~is still~~remains sensitive to ~~sudden~~abrupt changes in appearance, such as ~~significant differences~~substantial variations in snow cover or alterations in surface morphology due to e.g., extensive rockfalls. This issue was also highlighted as a major limitation by Kenner et al. (2018). However, because the algorithm can quickly process large amounts of data, we can leverage the full temporal resolution, allowing tracking to succeed as long as snow cover changes gradually, as shown in Figure ~~3D~~3d.

Another important limitation of our approach is that PIPs++ does not perform well in detecting movements for every pixel in the image due to the use of a regular grid compared to other frame-to-frame approaches. Currently, a regular grid size of ~~2 000~~2000 points per image is used, limited by computational power. While PIPs++ works well with the low-resolution images in this study, higher-resolution images quickly reach the limits of our available computational resources. One major limitation is the need for specific and expensive computational setups (e.g., an NVIDIA RTX A6000 GPU with 48GB). Even with these resources, increasing the temporal window, image resolution, and tracked points can quickly hit the limits. Considering appropriate GPU and CPU computational power, around ~~30~~15 min ~~were~~was needed to process the example dataset of this paper in an end-to-end fashion, from raw time-lapse images to velocity graphs. The majority of this time is needed to scale the output of the PIPs++ model with GIRAFFE, which is highly dependent on the size of the 3D point cloud.

~~Despite these limitations, we are confident that ongoing developments in AI processing will resolve these issues in the near future, making it possible to run AI frameworks on CPU only. Unlike PIPs++, the image-to-geometry approach does not require a GPU and can be performed on a laptop. However, to scale the time-lapse image data accurately, at least one UAV data survey is essential, and the quality of this scaling relies heavily on the quality of the UAV data. Additionally, a suboptimal oblique viewing angle, such as with Wcam05 (Fig. 1B~~

Ideally, the 3D point cloud used in GIRAFFE for image-to-geometry registration reflects the imaging situation at the time of the time-lapse image measurements, thereby avoiding intersection errors resulting from significant changes in surface topography between the image acquisition and the measurement of the reference data set (Fig. 8). Despite the temporal gap of approximately one year between the time-lapse image subsets and the 3D data, we assume that the overall topography has remained largely unchanged. Moreover, significant errors arising from potential discrepancies between the image content and the 3D surface are expected to be rejected in the outlier analyses in GIRAFFE. Such mismatches are unlikely to align with the

645 estimated camera model, as the model calculation relies on pseudo-control points that are more evenly distributed and exhibit strong agreement between the image content and the object surface. Nevertheless, minor inaccuracies caused by isolated structural changes (e.g., displacement of boulders) cannot be entirely ruled out. Such discrepancies can only be identified when analysing the movement trajectories as a whole. Furthermore, the quality of the image-based 3D trajectories is heavily correlated to the quality of the UAV data.

650
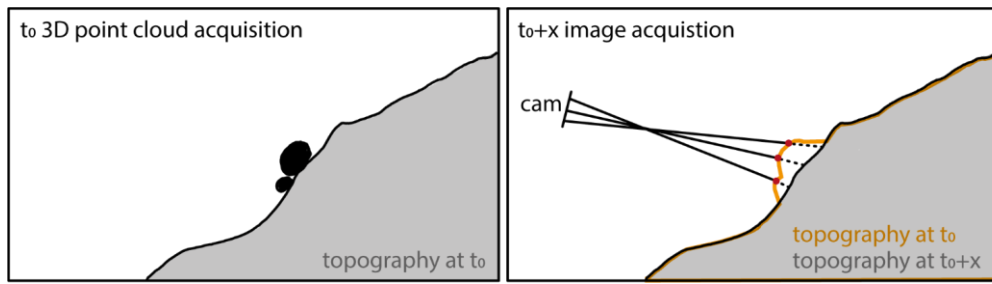
Figure 8: Illustration of the georeferencing validity issue when using a 3D point cloud acquired at time t_0 to transfer image measurements from a time-lapse image captured after significant topographic changes. In this example, boulders present during the initial 3D data acquisition are since been gone. Consequently, image rays intersect the outdated modelled topography, resulting in
655 **erroneous coordinates. These errors propagate into derived 3D trajectories and velocities. The greater the topographic changes between the reference data and affected image measure, the larger the error. Therefore, the reference topography should ideally reflect the conditions at the time of image acquisition.**

Additionally, a suboptimal oblique viewing angle, such as with Wcam05 (Fig. 1b), can complicate the matching process, as
660 the rendered view will be limited to a narrow strip. This can affect the distribution of matches and compromise the estimation of the camera's interior orientation and lens distortions (Elias et al., 2019). ~~Furthermore, our current assumption that the cameras remain stable over time justifies using a single image to determine the interior and exterior camera properties. However, for future work, it would be more accurate to perform this estimation for each image individually, as can be done with a stereoscopic camera system (Ioli et al., 2024), to account for temperature-induced variations (Elias et al., 2020).~~

665

~~**4.3 Outlook**~~

There is still potential to ~~optimize~~optimise the proposed workflow to achieve full automation for processing entire image sequences. This includes automatically detecting moving and stable areas, which currently relies on user defined criteria and thus depends on prior site knowledge. ~~Further enhancements to the image-to-geometry algorithm are necessary to increase its~~
670 ~~speed and computational efficiency for scaling several hundred timestamps simultaneously.~~ Additionally, we need to conduct

further investigations into the in-field calibration of intrinsic camera parameters ~~and their stability over time (Elias et al., 2020)~~, especially the image distortion, and their stability over time (Elias et al., 2020). This analysis aims to determine if it significantly enhances the quality of scaled results, similar to the benefits that are expected when using multiple epochs of UAV data for updating the camera calibration. Improvements in 2D to 3D tools (~~image to geometry registration~~like

GIRAFFE) could also benefit other disciplines, such as the quantitative analysis of historical terrestrial photographs for mapping historical rockfall (Wegner et al., 2023) and changes in glacier forefields (Altmann et al., 2020).

Moreover, additional research is necessary to evaluate whether AI-based tracking algorithms like PIPs++ could effectively track landform velocities using aerial datasets such as consecutive UAV orthophotos or satellite imagery. Furthermore, the developed workflow could prove valuable for analysing monoscopic time-lapse image sequences of other dynamic processes, such as lava flows (James and Robson, 2014), solifluction and gelifluction movements (Matsuoka, 2014), and flow velocities in rivers ~~(Eltner et al., 2020; Stumpf et al., 2016)~~(Eltner et al., 2020; Stumpf et al., 2016). Given the prevalence of time-lapse camera data collection, a rapid and efficient method for automatically processing such extensive datasets holds significant scientific relevance. Furthermore, the fast and robust processing of the time-lapse imagery makes it possible to function as an early-warning system when processing can be carried out in near real-time, as indicated by ~~Kenner et al. (2018)~~Kenner et al. (2018).

~~5.~~6 Conclusion

This proof-of-concept demonstrates the potential of AI-based algorithms for tracking and matching points to improve motion estimations in time-lapse image sequences of a mountain landscape. ~~Our pilot study opens the door to processing entire image datasets to reveal spatio-temporal patterns that traditional monitoring methods have previously overlooked due to their limited spatial or temporal resolution.~~Two fast-moving alpine landforms - a landslide and a rock glacier at the Grabengufer site in Switzerland - were selected as the pilot study area. The initial results presented in this paper show that robust and reliable velocity information can be quickly derived with minimal input data and user intervention. Our pilot study opens the door to processing entire image datasets to reveal spatio-temporal patterns that traditional monitoring methods have previously overlooked, due to their limited spatial or temporal resolution and the inadequate computational and algorithmic power to handle large image datasets.

The PIPs++ model, used for tracking features in image sequences, excels in widening the temporal window and includes a template-update mechanism that allows for changes in feature appearance. Its key advantage is its ability to accurately estimate occluded trajectories within the temporal frame, avoiding suboptimal matches and enhancing tracking accuracy, making it especially robust for environmental applications and eliminates the need for filtering blurry or foggy images as a pre-processing step. Additionally, the model's rapid performance—, processing 400 images in two minutes to track features through a temporal window of 19 frames ~~on an NVIDIA RTX A6000~~, is promising for handling large datasets and developing early-warning systems.

The image-to-geometry approach, implemented in GIRAFFE, provides an accurate way to scale the 2D image data into ~~a~~ 3D object space, even under suboptimal camera viewing angles and distance to the area of interest. Future research will focus on ~~enhancing the image-to-geometry algorithm for efficient scaling of multiple timestamps,~~ in-field camera calibration~~,~~ and evaluating the potential benefits of using multiple epochs of UAV data.

This paper represents an important step forward in using monoscopic cameras and leveraging previously captured data that have not been processed automatically with metric values before. By significantly enhancing temporal acquisition frequency using basic time-lapse imagery with zero cost, we can achieve a level of data resolution that would be expensive with in-situ differential Global Navigation Satellite System (GNSS) and georeferenced Total Station (TS) measurements or ~~UAV~~Uncrewed Aerial Vehicles and Terrestrial or Airborne Laser Scanning methods. Validated by discrete ~~theodolite,~~ ~~GNSS,~~TS and ~~continuous fixed~~in-situ GNSS measurements, our approach provides a spatially continuous understanding of landform movement. It allows data acquisition in areas where in-situ measurements are impractical due to logistical and safety constraints, and where other remote sensing techniques fail due to high landform displacements. Furthermore, depending on the image resolution, distance to the landform, and its velocity, our approach can achieve a sub-seasonal resolution of velocity information with an accuracy of several cm.

This study introduces a new open-source tool for scientists to automatically extract ~~velocity~~metric information from existing webcam datasets, extending its applicability to various phenomena, including lava flows, water flows, and creeping landforms such as landslides, rock glaciers, and solifluction lobes.

Code availability

Part of this work is based on existing algorithms, available under https://github.com/aharley/pips2 for PIPs++ tracker and https://github.com/cvg/LightGlue for LightGlue matching algorithm. GIRAFFE is available under https://github.com/mel-ias/GIRAFFE. The code used for this proof-of-concept is partly available under https://github.com/hannehendrickx/pips_env. Please follow this repository to receive further updates. All code is available upon reasonable request to the corresponding author. We encourage people with similar monoscopic time-lapse image datasets to reach out to the authors.

Data availability

The sample ~~used in this paper~~ (images~~)~~ and ~~respective outputs (~~corresponding trajectory files~~) can be found here~~ used in this study are available at: https://github.com/hannehendrickx/pips_env~~.~~ and at Zenodo (doi:10.5281/zenodo.14260180) along with sample files that need to be set up according to the GIRAFFE documentation in order to run the tool. For an up-to-date overview of the sites, including the latest webcam images, please visit the following pages: Grabengufer Landslide and Grabengufer Rock Glacier.

Author contribution

HH, XB~~, ME~~ and AE designed the research. HH, XB ~~and ME created~~developed the Python ~~and CC++ codes used in this paper.~~code for running PIPs++ on the time-lapse images. ME developed GIRAFFE for image-to-geometry registration and the python code for stabilising image sequences. HH, ME prepared and processed data, made all the figures and wrote the initial version of the paper. ~~ME processed data with the image-to-geometry code and provided input for the writing of those respective sections.~~ RD conducted field investigations and provided field specific knowledge to aid the writing process. All authors improved and revised the initial manuscript.

Competing interests

The authors declare no conflicts of interests.

Acknowledgments

~~The authors would like to thank Sebastian Pfaehler (University of Fribourg, CH) for the capturing and processing of the UAV data used in this study.~~
The authors thank Sebastian Pfaehler (University of Fribourg, CH) for capturing and processing the UAV data, and Sebastian Summermatter and Martin Volken (Geomatik AG / Planax AG) for the collection and processing of the total station data. We acknowledge the support of the municipality of Randa and the Canton of Valais (Service for Natural Hazards) in facilitating the field investigations. Geosat SA is acknowledged for setting up the in-situ GNSS devices and handling data processing, and we thank the Canton of Valais for providing access to the in-situ GNSS data. We also acknowledge Idelec SA for their assistance with webcam maintenance. We would like to thank the numerous collaborators at the University of Fribourg for their contributions to the data processing, webcam maintenance, and image transfer and archiving. Air Zermatt is also thanked for ensuring safe transport to and from the site.
ChatGPT was ~~utilized~~utilised as a tool in this study to assist ~~in~~with coding ~~for this study. Additionally, ChatGPT contributed to enhancing~~and to enhance the English language quality of ~~this~~the manuscript through text input. ~~It is important to note that ChatGPT~~It was not employed to generate original text ~~from scratch at any point~~ during the research process.

References

Altmann, M., Piermattei, L., Haas, F., Heckmann, T., Fleischer, F., Rom, J., Betz-Nutz, S., Knoflach, B., Müller, S., Ramskogler, K., Pfeiffer, M., Hofmeister, F., Ressl, C., and Becht, M.: Long-Term Changes of Morphodynamics on Little Ice Age Lateral Moraines and the Resulting Sediment Transfer into Mountain Streams in the Upper Kauner Valley, Austria, Water 2020, Vol. 12, Page 3375, 12, 3375, https://doi.org/10.3390/W12123375, 2020.

Glaciorisk - L'innovation digitale au service des dangers naturels: https://www.glaciorisk.ch/, last access: 17 July 2024.

Barsch, D.: Rockglaciers, Springer Berlin Heidelberg, Berlin, Heidelberg, https://doi.org/10.1007/978-3-642-80093-1, 1996.

Blanch, X., Guinau, M., Eltner, A., ~~Guinau, M.,~~ and Abellan, A.: ~~Multi-epoch and multi-imagery (Memi)~~Fixed photogrammetric ~~workflow~~systems for ~~enhanced change detection using time lapse cameras, Remote Sensing, 13~~natural hazard monitoring with high spatio-temporal resolution, Natural Hazards and Earth System Sciences, 23, 3285–3303, https://doi.org/10.~~3390/rs13081460, 2021~~5194/nhess-23-3285-2023, 2023.

Cicoira, A., Marcer, M., Gärtner-Roer, I., Bodin, X., Arenson, L. U., and Vieli, A.: A general theory of rock glacier creep based on in-situ and remote sensing observations, Permafrost and Periglacial Processes, 32, 139–153, https://doi.org/10.1002/ppp.2090, 2021.

Cicoira, A., Weber, S., Biri, A., Buchli, B., Delaloye, R., Da Forno, R., Gärtner-Roer, I., Gruber, S., Gsell, T., Hasler, A., Lim, R., Limpach, P., Mayoraz, R., Meyer, M., Noetzli, J., Phillips, M., Pointner, E., Raetzo, H., Scapozza, C., Strozzi, T., Thiele, L., Vieli, A., Vonder Mühll, D., Wirz, V., and Beutel, J.: In situ observations of the Swiss periglacial environment using GNSS instruments, Earth System Science Data, 14, 5061–5091, https://doi.org/10.5194/essd-14-5061-2022, 2022.

Delaloye, R~~. and Staub, B.: Seasonal variations of rock glacier creep: Time series observations from the Western Swiss Alps, in: XI. International Conference On Permafrost – Book of Abstracts, Bibliothek Wissenschaftspark Albert Einstein, 24 June 2016, Potsdam, Germany, 2016.~~

~~Delaloye, R.~~, Lambiel, C., and Gärtner-Roer, I.: Overview of rock glacier kinematics research in the Swiss Alps: seasonal rhythm, interannual variations and trends over several decades, Geographica Helvetica, 65, 135–145, https://doi.org/10.5194/gh-65-135-2010, 2010.

Delaloye, R., Morard, S., Barboux, C., Abbet, D., Gruber, V., Riedo, M., and Gachet, S.: Rapidly moving rock glaciers in Mattertal, Jahrestagung der Schweizerischen Geomorphologischen Gesellschaft, 21–31, 2013.

Elias, M., Kehl, C., and Schneider, D.: Photogrammetric water level determination using smartphone technology, The Photogrammetric Record, 34, 198–223, https://doi.org/10.1111/phor.12280, 2019.

Elias, M., Eltner, A., Liebold, F., and Maas, H.-G.: Assessing the Influence of Temperature Changes on the Geometric Stability of Smartphone- and Raspberry Pi Cameras, Sensors, 20, 643, https://doi.org/10.3390/s20030643, 2020.

Elias, M., and Maas, H.-G.: Measuring Water Levels by Handheld Smartphones – A contribution to exploit crowdsourcing in the spatio temporal densification of water gauging networks, The International Hydrographic Review, 27, 9–22, https://doi.org/10.58440/ihr-27-a01, 2022.

Elias, M., Weitkamp, A., and Eltner, A.: Multi-modal image matching to colorize a SLAM based point cloud with arbitrary data from a thermal camera, ISPRS Open Journal of Photogrammetry and Remote Sensing, 9, 100041, https://doi.org/10.1016/j.ophoto.2023.100041, 2023.

Elias, M., Isfort, S., Eltner, A., and Maas, H.-G.: UAS Photogrammetry for Precise Digital Elevation Models of Complex Topography: A Strategy Guide, ISPRS Ann. Photogramm. Remote Sens. Spatial Inf. Sci., X-2-2024, 57–64, https://doi.org/10.5194/isprs-annals-X-2-2024-57-2024, 2024.

Eltner, A., Kaiser, A., Abellan, A., and Schindewolf, M.: Time lapse structure-from-motion photogrammetry for continuous geomorphic monitoring, Earth Surface Processes and Landforms, 42, 2240–2253, https://doi.org/10.1002/esp.4178, 2017.

Eltner, A., Sardemann, H., and Grundmann, J.: Technical Note: Flow velocity and discharge measurement in rivers using terrestrial and unmanned-aerial-vehicle imagery, Hydrology and Earth System Sciences, 24, 1429–1445, https://doi.org/10.5194/hess-24-1429-2020, 2020.

Eltner, A., Hoffmeiste, D., Kaiser, A., Karrasch, P., Klingbeil, L., Stöcker, C., and Rovere, A.: UAVs for the Environmental Sciences, 494 pp., 2022.

Fortun, D., Bouthemy, P., and Kervrann, C.: Optical flow modeling and computation: A survey, Computer Vision and Image Understanding, 134, 1–21, https://doi.org/10.1016/j.cviu.2015.02.008, 2015.

Frauenfelder, R., Haeberli, W., and Hoelzle, M.: Rockglacier occurrence and related terrain parameters in a study area of the Eastern Swiss Alps, Permafrost`, 253–258, 2003.

Harley, A. W., Fang, Z., and Fragkiadaki, K.: Particle Video Revisited: Tracking Through Occlusions Using Point Trajectories, 2022.

He, K., Zhang, X., Ren, S., and Sun, J.: Deep Residual Learning for Image Recognition, in: 2016 IEEE Conference on Computer Vision and Pattern Recognition (CVPR), 2016 IEEE Conference on Computer Vision and Pattern Recognition (CVPR), Las Vegas, NV, USA, 770–778, https://doi.org/10.1109/CVPR.2016.90, 2016.

Heid, T. and Kääb, A.: Evaluation of existing image matching methods for deriving glacier surface displacements globally from optical satellite imagery, Remote Sensing of Environment, 118, 339–355, https://doi.org/10.1016/j.rse.2011.11.024, 2012.

Hermle, D., Gaeta, M., Krautblatter, M., Mazzanti, P., and Keuschnig, M.: Performance Testing of Optical Flow Time Series Analyses Based on a Fast, High-Alpine Landslide, Remote Sensing, 14, https://doi.org/10.3390/rs14030455, 2022.

How, P., Hulton, N. R. J., Buie, L., and Benn, D. I.: PyTrx: A Python-Based Monoscopic Terrestrial Photogrammetry Toolset for Glaciology, Frontiers in Earth Science, 8, 2020.

Huang, Z., Shi, X., Zhang, C., Wang, Q., Cheung, K. C., Qin, H., Dai, J., and Li, H.: FlowFormer: A Transformer Architecture for Optical Flow, in: Computer Vision – ECCV 2022, Cham, 668–685, https://doi.org/10.1007/978-3-031-19790-1_40, 2022.

Hur, J. and Roth, S.: Optical Flow Estimation in the Deep Learning Age, in: Modelling Human Motion: From Human Perception to Robot Design, edited by: Noceti, N., Sciutti, A., and Rea, F., Springer International Publishing, Cham, 119–140, https://doi.org/10.1007/978-3-030-46732-6_7, 2020.

Ioli, F., Dematteis, N., Giordan, D., Nex, F., and Pinto, L.: Deep Learning Low-cost Photogrammetry for 4D Short-term Glacier Dynamics Monitoring, PFG, https://doi.org/10.1007/s41064-023-00272-w, 2024.

James, M. R. and Robson, S.: Sequential digital elevation models of active lava flows from ground-based stereo time-lapse imagery, ISPRS Journal of Photogrammetry and Remote Sensing, 97, 160–170, https://doi.org/10.1016/j.isprsjprs.2014.08.011, 2014.

Kääb, A. and Reichmuth, T.: Advance mechanisms of rock glaciers, Permafrost and Periglacial Processes, 16, 187–193, https://doi.org/10.1002/ppp.507, 2005.

Kääb, A. and Vollmer, M.: Surface Geometry, Thickness Changes and Flow Fields on Creeping Mountain Permafrost: Automatic Extraction by Digital Image Analysis, Permafrost and Periglacial Processes, 11, 315–326, https://doi.org/10.1002/1099-1530(200012)11:4<315::AID-PPP365>3.0.CO;2-J, 2000.

Kenner, R., Phillips, M., Limpach, P., Beutel, J., and Hiller, M.: Monitoring mass movements using georeferenced time-lapse photography: Ritigraben rock glacier, western Swiss Alps, Cold Regions Science and Technology, 145, 127–134, https://doi.org/10.1016/j.coldregions.2017.10.018, 2018.

835 Kummert, M. and Delaloye, R.: Mapping and quantifying sediment transfer between the front of rapidly moving rock glaciers and torrential gullies, Geomorphology, 309, 60–76, https://doi.org/10.1016/j.geomorph.2018.02.021, 2018.

Kummert, M., Delaloye, R., and Braillard, L.: Erosion and sediment transfer processes at the front of rapidly moving rock glaciers: Systematic observations with automatic cameras in the western Swiss Alps, Permafrost and Periglacial Processes, 29, 21–33, https://doi.org/10.1002/ppp.1960, 2018.

840 Lindenberger, P., Sarlin, P.-E., and Pollefeys, M.: LightGlue: Local Feature Matching at Light Speed, in: ICCV, 2023.

Lowe, D. G.: Distinctive Image Features from Scale-Invariant Keypoints, International Journal of Computer Vision, 60, 2, 91–110, https://doi.org/10.1023/B:VISI.0000029664.99615.94

Marcer, M., Bodin, X., Brenning, A., Schoeneich, P., Charvet, R., and Gottardi, F.: Permafrost Favorability Index: Spatial Modeling in the French Alps Using a Rock Glacier Inventory, Frontiers in Earth Science, 5, 105,
845 https://doi.org/10.3389/feart.2017.00105, 2017.

Marcer, M., Cicoira, A., Cusicanqui, D., Bodin, X., Echelard, T., Obregon, R., and Schoeneich, P.: Rock glaciers throughout the French Alps accelerated and destabilised since 1990 as air temperatures increased, Communications Earth & Environment, 2, 1–11, https://doi.org/10.1038/s43247-021-00150-6, 2021.

Matsuoka, N.: Combining Time-Lapse Photography and Multisensor Monitoring to Understand Frost Creep Dynamics in the
850 Japanese Alps, Permafrost and Periglacial Processes, 25, 94–106, https://doi.org/10.1002/ppp.1806, 2014.

Pellet, C., Bodin, X., Cusicanqui, D., Delaloye, R., Kaab, A., Kaufmann, V., Noetzli, J., Thibert, E., Vivero, S., and Kellerer-Pirklbauer, A.: State of the climate in 2022: Rock glaciers velocity, Bulletin of the American Meteorological Society, 104, 41–42, https://doi.org/10.1175/2023BAMSStateoftheClimate.1, 2023.

RGIK, R. glacier inventories and kinematics: Guidelines for inventorying rock glaciers: baseline and practical concepts
855 (Version 1.0), https://doi.org/10.51363/unifr.srr.2023.002, 2023.

Sarlin, P. E., Detone, D., Malisiewicz, T., and Rabinovich, A.: SuperGlue: Learning Feature Matching with Graph Neural Networks, Proceedings of the IEEE Computer Society Conference on Computer Vision and Pattern Recognition, 4937–4946, https://doi.org/10.1109/CVPR42600.2020.00499, 2020.

Schwalbe, E. and Maas, H.-G.: The determination of high-resolution spatio-temporal glacier motion fields from time-lapse
860 sequences, Earth Surface Dynamics, 5, 861–879, https://doi.org/10.5194/esurf-5-861-2017, 2017.

Shi, X., Huang, Z., Bian, W., Li, D., Zhang, M., Cheung, K. C., See, S., Qin, H., Dai, J., and Li, H.: VideoFlow: Exploiting Temporal Cues for Multi-frame Optical Flow Estimation, https://doi.org/10.48550/arXiv.2303.08340, 20 August 2023.

Stumpf, A., Augereau, E., Delacourt, C., and Bonnier, J.: Photogrammetric discharge monitoring of small tropical mountain rivers: A case study at Rivière des Pluies, Réunion Island, Water Resources Research, 52, 4550–4570,
865 https://doi.org/10.1002/2015WR018292, 2016.

Sun, J., Shen, Z., Wang, Y., Bao, H., and Zhou, X.: LoFTR: Detector-Free Local Feature Matching with Transformers, Proceedings of the IEEE Computer Society Conference on Computer Vision and Pattern Recognition, 4, 8918–8927, https://doi.org/10.1109/CVPR46437.2021.00881, 2021.

Teed, Z. and Deng, J.: RAFT: Recurrent All-Pairs Field Transforms for Optical Flow, in: Computer Vision – ECCV 2020, Cham, 402–419, https://doi.org/10.1007/978-3-030-58536-5_24, 2020.

Travelletti, J., Delacourt, C., Allemand, P., Malet, J.-P., Schmittbuhl, J., Toussaint, R., and Bastard, M.: Correlation of multi-temporal ground-based optical images for landslide monitoring: Application, potential and limitations, ISPRS Journal of Photogrammetry and Remote Sensing, 70, 39–55, https://doi.org/10.1016/j.isprsjprs.2012.03.007, 2012.

Ulm, M., Elias, M., Eltner, A., Lotsari, E., and Anders, A.: Automated change detection in photogrammetric 4D point clouds – Transferability and extension of 4D objects-by-change for monitoring riverbank dynamics using low-cost cameras, Proceedings of the 6th Joint International Symposium on Deformation Monitoring (JIDSM), 2025-April, 1–8, in press, 2025.

Wegner, K., Stark, M., Haas, F., and Becht, M.: Suitability of terrestrial archival imagery for SfM-MVS based surface reconstruction of steep rock walls for the detection of rockfalls, Journal of Geomorphology, https://doi.org/10.1127/jgeomorphology/2023/0775, 2023.

Xu, H., Zhang, J., Cai, J., Rezatofighi, H., and Tao, D.: GMFlow: Learning Optical Flow via Global Matching, Proceedings of the IEEE Computer Society Conference on Computer Vision and Pattern Recognition, 2022-June, 8111–8120, https://doi.org/10.1109/CVPR52688.2022.00795, 2022.

Zheng, Y., Harley, A. W., Shen, B., Wetzstein, G., and Guibas, L. J.: PointOdyssey: A Large-Scale Synthetic Dataset for Long-Term Point Tracking, 2023.